Chin. J. Astron. Astrophys. Vol. 6 (2006), **Suppl. 1**, 269–278
(*http://www.chjaa.org*)

Chinese Journal of
Astronomy and
Astrophysics

Microquasars: What do radio and X-ray observations tell us?

Diana C. Hannikainen[1 ⋆], Kinwah Wu[2], Jason A. Stevens[3], Osmi Vilhu[1], Jérôme Rodriguez[4], Linnea Hjalmarsdotter[1] and Richard W. Hunstead[5]

[1] Observatory, PO Box 14, FIN-00014 University of Helsinki, Finland
[2] MSSL, UCL, Holmbury St. Mary, Surrey, RH5 6NT, UK
[3] University of Hertfordshire, UK
[4] Centre d'Etudes de Saclay, 91191 Gif-sur-Yvette Cedex, France
[5] School of Physics, University of Sydney, NSW 2006, Australia

Abstract Microquasars, or X-ray binaries exhibiting radio jets, have been observed extensively at all wavelengths for the past decade or so. Primarily, they have been observed in the X-ray regimes and the radio. In this paper we review the radio and the X-ray behavior of the first two superluminal microquasars, GRS 1915+105 and GRO J1655−40. We show how GRO J1665−40 really *does* behave like a "micro"-quasar based on the similarity of the radio properties between the source and quasars, and we also show some recent X-ray/γ-ray results obtained with *INTEGRAL* and *RXTE* on the notorious microquasar, GRS 1915+105.

Key words: X-ray binaries – observations: radio – observations: X-ray – observations: γ-ray

1 INTRODUCTION

X-ray binaries have been studied extensively since Scorpius X-1 was discovered in 1962 by Riccardo Giacconi (Giacconi et al. 1962). X-ray binaries consist of a compact object – either a neutron star or a black hole – feeding from a non-degenerate companion. The companion determines whether the X-ray binary is a high-mass or a low-mass X-ray binary – for high-mass X-ray binaries the companion is a massive OB star or a supergiant, whereas for low-mass X-ray binaries the companion is a lower main sequence star or a red giant.

In both cases, the accretion of matter from the non-degenerate companion onto the compact object is the source of the X-ray emission. The accreted matter does not fall straight onto the surface (when the compact object is a neutron star) or directly into the black hole, but forms an accretion disk around the compact object. This accretion disk is responsible for the soft X-ray ($\sim$2–10 keV) emission. When there is a corona (i.e. a hot plasma cloud) surrounding the inner portions of the accretion disk, it can upscatter – via the inverse Compton process – the low energy photons to high energy photons ($>$ 20 keV).

In the past 15 years or so, a new phenomenon has been observed in X-ray binaries, and that is the outflow of matter in the form of jets (whether the outflow is continuous or in "blobs" is to be discussed later). This outflow gives rise to synchrotron radiation and hence is observed in the radio.

Quasars have also been observed at all wavelengths since their discovery in the 1960's. They are composed of a supermassive black hole ($10^6 - 10^9\ M_\odot$) accreting matter from their host galaxy. What makes these objects remarkable (apart from the huge black hole at their centers) are their outflows which can be several million lightyears in length and which seem to emanate from the central source at apparently superluminal velocities.

It was the similarity in morphology – especially the discovery of apparent superluminal motion in the jets of X-ray binaries – that suggested the name "microquasar" for the radio-emitting X-ray binaries. The

⋆ E-mail: `diana@astro.helsinki.fi`

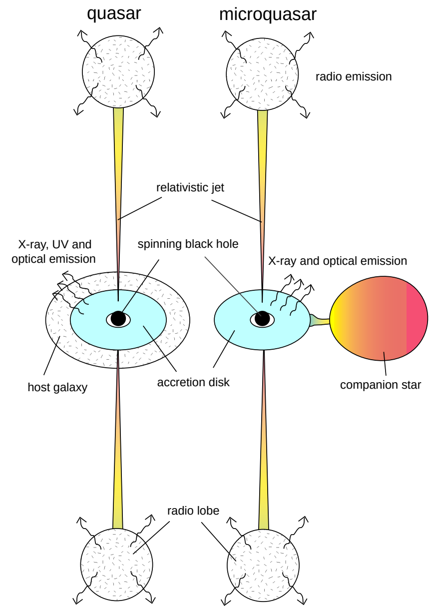

Fig. 1 A schematic illustration showing the similarity between microquasars and AGN/quasars (adapted from Mirabel & Rodríguez 1998).

two sources – quasars and microquasars – share three (at least) common ingredients: a central black hole accreting matter and then ejecting it at nearly the speed of light. In the case of quasars, the black hole is *supermassive* and it accretes from the host galaxy. In the case of microquasars, it is a *stellar-mass* black hole accreting matter from the companion star. Figure 1 shows the similarity in configurations of the two types of systems.

Recently, all manner of correlations have been discovered in microquasars between the radio and the X-ray (e.g. Hannikainen et al. 1998; Gallo, Fender & Pooley 2003). Here we are not going to discuss all the detailed observations and phenomenology of all the microquasars, but instead we shall concentrate on the two well known sources – the notorious GRS 1915+105 and the second Galactic source found to exhibit superluminal motion GRO J1655−40 – and see what can be achieved with intensive radio monitoring over several weeks for the latter and complete X-ray coverage during one day for the former. We will show that *microquasars* are indeed *micro*-quasars and how complex variability can be deciphered. This paper is divided into two parts: First we start with the discussion on the radio emission from GRO J1655−40 and continue with X-ray/gamma-ray observations of GRS 1915+105.

2 GRO J1655−40

2.1 The Radio Properties of Compact Extragalactic Sources

Compact extragalactic sources often show powerlaw spectra at high frequencies (>90 GHz; see e.g. Gear et al. 1994). In addition, high levels of linear polarization are often observed. These two together provide strong evidence for optically thin synchrotron emission from non-thermal relativistic electrons. The spectra of many sources also show a turnover at low frequencies, which is generally attributed to optical depth effects: the radiation is self-absorbed and becomes opaque below a critical frequency.

2.2 Bubbles vs. Shocks

Traditionally, the temporal evolution of the low frequency radio spectra was explained qualitatively by the "synchrotron bubble" model (van der Laan 1966; Hjellming & Johnston 1988). But this model failed to fully explain the behavior at low frequencies. With more observations at higher frequencies, it soon became apparent that the model failed totally to reproduce even the qualitative behavior of the sources. A new model invoking shocks that accelerate electrons to relativistic energies as they propagate along the jets was formulated (Marscher & Gear 1985). Below we briefly describe these two models and show why the "shock" model is more acceptable in describing the radio behavior of extragalactic sources and how it is also the preferable model to describe the radio emission from microquasars.

2.2.1 The Synchrotron Bubble Model

In this model, the radio emission is assumed to be emitted from a cloud composed of relativistic electrons and a randomly oriented magnetic field. The energy densities of the relativistic electrons and the magnetic field are in equipartition. The radiative process is relatively inefficient such that the electrons and magnetic field lose energy due to the (quasi-)adiabatic expansion of the cloud. This model predicts that the emission at the high frequencies peaks before the low frequencies, and the peak flux density is higher for the higher frequencies and subsequently lower for the lower frequencies. This is illustrated in Figure 2 left. The spectrum is inverted and self-absorbed initially, and then becomes optically thin and appears as a powerlaw as the cloud or bubble expands, which is shown in Figure 2 right. In both cases the flus density S_ν are calculated according to the prescription given in Hjellming & Johnston (1988).

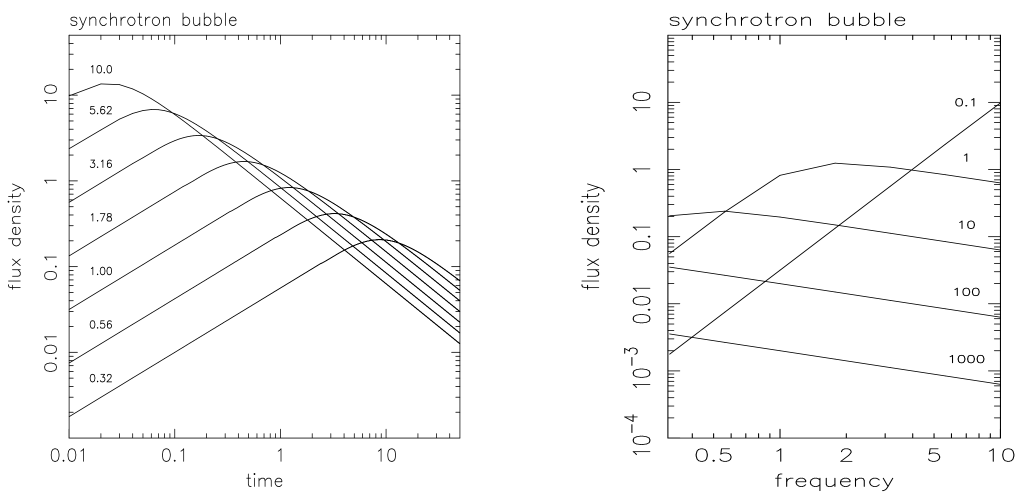

Fig. 2 *Left.* The multi-frequency lightcurves of the synchrotron bubble model. The radio emitting region is assumed to be spherical and the relativistic electrons have an energy distribution $N(E) \propto E^{-s}$, where $s = 2$. The normalization is such that $S_\nu = 1$ for frequency $\nu = 1$. The frequencies are shown in the plot. *Right.* The spectra of the synchrotron bubble model. Shown in the plot are arbitrary times.

2.2.2 The Generalized Shock Model

This model consists of an adiabatic relativistic jet in which transverse shock waves form in response to changes in pressure or bulk flow (e.g. Blandford & Königl 1979; Marscher & Gear 1985). The evolution of the shock is described in terms of the flux density at the peak frequency of the synchrotron spectrum where the opacity is close to unity – this point is determined at any moment by the dominant loss mechanism.

• inverse-Compton losses predominate when the emitting region is compact

– *Compton or growth stage*

• as the shock region expands, synchrotron losses dominate

– *synchrotron or plateau stage*

• losses are due to adiabatic expansion, as the shock expands even further and the radiative lifetime of of the electrons becomes long with respect to the time needed to traverse the region

— *adiabatic or decay stage*

These model predictions for the spectral evolution during flaring events are shown in Figure 3.

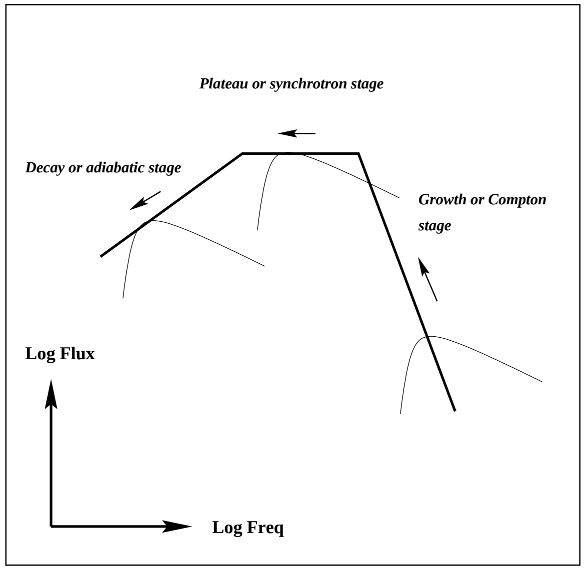

Fig. 3 Schematic representation of the generalised-shock model proposed by Marscher & Gear (1985). The development of the shock can be characterized by the growth, plateau, and decay stages.

What this all means is that the maximum flare amplitude for any frequency on the Compton stage occurs when the spectrum transits onto the synchrotron stage (see Valtaoja et al. 1992 for a detailed description). Lightcurves at such frequencies are thus predicted to peak simultaneously and because of the spectral shape, the flare amplitudes are expected to increase towards lower frequencies. Specifically, they should have the same powerlaw form as the optically thin portion of the flare spectrum. Flare amplitudes are expected to be approximately constant during the synchrotron stage and to decrease during the adiabatic stage. The lightcurves will display time-lagged behavior with a delay between any two frequencies equal to the time taken for the spectrum to evolve between them and become optically thin.

2.3 Introduction to GRO J1655$-$40

GRO J1655$-$40 was the second Galactic source to be discovered which exhibited apparent superluminal motion. GRO J1655$-$40 is a black hole binary with an evolved F-type star (Orosz & Bailyn 1997; Soria et al. 1998). The unseen companion has a mass $M_x > 5.1\ M_\odot$ (Soria et al. 1998) confirming the black hole nature of this binary. In 1994 GRO J1655$-$40 showed a dramatic radio outburst: the flux density at 843 MHz increased from a few hundred mJy to ∼8 Jy in about 13 days (Hannikainen et al. 2000). VLBA images taken during the outburst show collimated, relativistic jets (e.g. Hjellming & Rupen 1995). Once corrected for relativistic effects, the velocity of the jets was $\sim 0.92c$.

2.4 Radio Monitoring Observations

The 1994 radio outburst of GRO J1655$-$40 was monitored with several telescopes — the Very Large Array (Hjellming & Rupen 1995), and the Australia Telescope Compact Array and the Molonglo Observatory Synthesis Telescope (Hannikainen et al. 2000), the data of the latter two are reproduced here. The outburst shows complex flaring behavior, seen in the multi-frequency lightcurves (Fig. 4, left). There are several minor events following the initial increase in flux. The key features are that the initial rise in flux peaks simultaneously at all frequencies and that the amplitude of the flare, which is maximum minus the minimum flux, increases toward lower frequency (Fig. 4, right). In addition, both linear (Hannikainen et al. 2000) and circular polarization (Macquart et al. 2002) were observed.

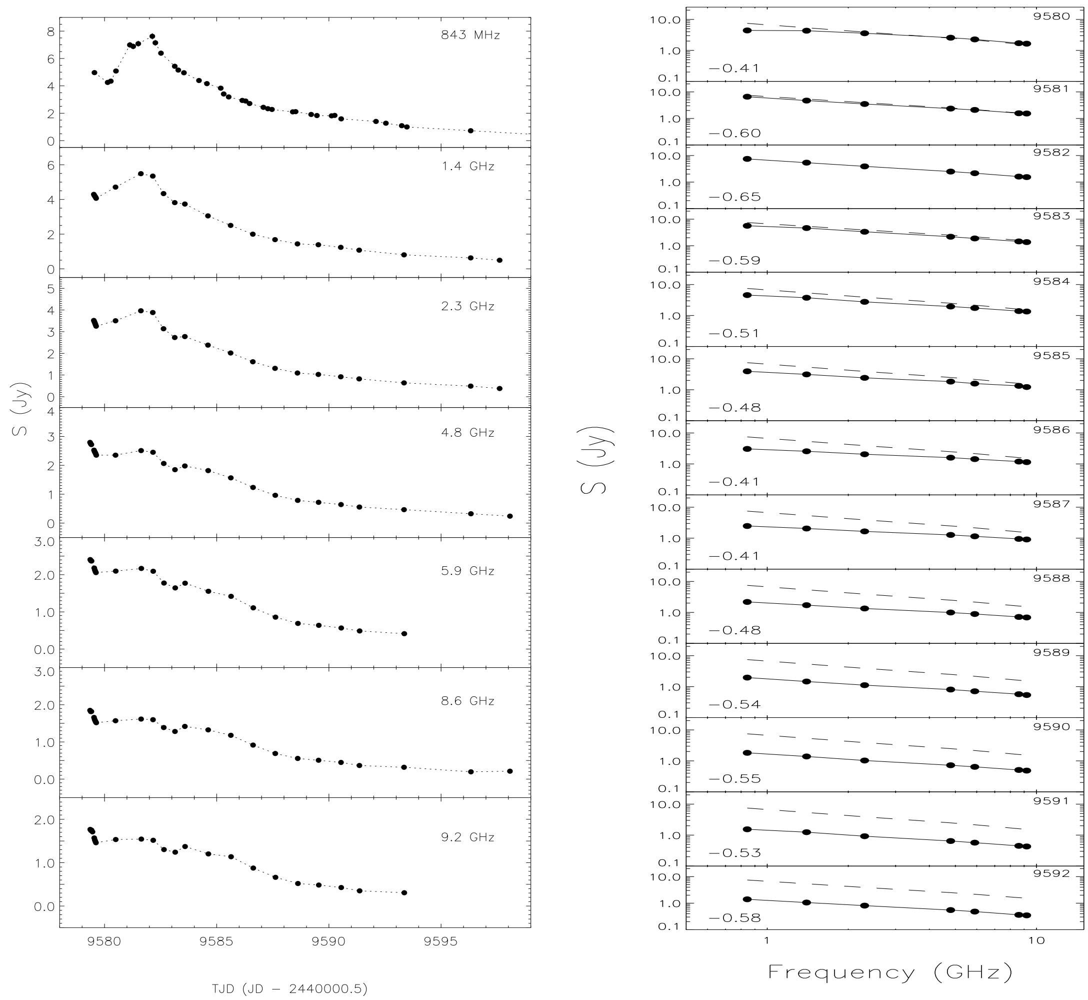

Fig. 4 *Left.* The multi-frequency radio lightcurves of GRO J1655−40 during the 1994 outburst. *Right.* The radio spectra from the same time. The dashed lines are the spectra at TJD 9582 (shown as a reference to illustrate the spectral evolution. The two-point (highest and lowest frequencies) spectral indices are shown in the lower corner of each sub-panel.

2.5 Results and Discussion

The radio spectrum can be described as a powerlaw most of the time, but it becomes inverted when flaring begins (Hannikainen et al. 2000). The spectrum just before flux maximum (Fig. 4, right panel, top) is consistent with a synchrotron spectrum which is optically thin at the highest frequencies but becomes self-absorbed at around 1 GHz. As flaring proceeds, the entire spectrum becomes optically thin and remains so throughout the subsequent decline in flux density. From the two-point spectral indices, we can see that the spectrum flattens as the flux initially declines. It then steepens again at the onset of the second outburst, as can be seen in Hannikainen et al. (2000). A possible explanation is that the emission arises from several regions, as proposed by Hannikainen et al. (2000). They evoke a phenomenological model in which the emission comes from both an extended lobes and a compact core.

The figures clearly show that the time-dependent spectral properties of the 1994 outburst of GRO J1655−40 contradict the prediction of the synchrotron bubble model. Instead, the behavior can be easily explained by the generalised-shock model. The simultaneous peaking of the lightcurves at all frequencies is consistent with the properties of the Compton/growth stage if the transition from the synchrotron/plateau stage is at a frequency lower than the frequencies of the observation. The flare amplitudes fall off as a powerlaw at the Compton/growth stage, and they have the same frequency dependence until it reaches the transition point between the growth and plateau stages. The flare amplitude of GRO J1655−40 is -0.69 (see Stevens et al. 2003), similar to the optically thin portion of the flare synchrotron spectrum of extragalactic sources. Hence we can truly say that GRO J1655−40 is indeed a "micro"-quasar.

3 GRS 1915+105

3.1 Introduction to the Source

GRS 1915+105 has been extensively observed at all wavelengths ever since its discovery. It was originally detected as a hard X-ray source with the WATCH all-sky monitor on the GRANAT satellite (Castro-Tirado et al. 1992). Apparent superluminal ejections have been observed from GRS 1915+105 several times with the VLA and with MERLIN (Rodríguez & Mirabel 1999; Fender et al. 1999). Both times the true ejection velocity was calculated to be $> 0.9c$. The mass-donating star is a K-M giant (Greiner et al. 2001), while the mass of the black hole has been calculated to be $14 \pm 4.0\ M_{\odot}$ (Harlaftis & Greiner 2004). These are in a binary orbit of 33.5 days. The Rossi X-ray Timing Explorer (*RXTE*) has observed GRS 1915+105 since its launch and has shown the source to be highly variable on all timescales from milliseconds to months (see e.g. Belloni et al. 2000). Belloni et al. (2000) categorized the variability into twelve distinct classes which they labelled with Greek letters and identified three distinct X-ray states: two softer states (A and B) and a harder state (C). Here we will discuss simultaneous *INTEGRAL* and *RXTE* observations of GRS 1915+105 and show how we defined a new class of variability.

3.1.1 Observations

The European Space Agency's INTErnational Gamma-Ray Astrophysical Laboratory (*INTEGRAL*) is aimed at observing the sky between ∼3 keV and 10 MeV (Winkler et al. 2003). The *INTEGRAL* payload consists of two gamma-ray instruments – IBIS and SPI, one X-ray monitor – JEM-X, and an optical monitor. GRS 1915+105 was monitored with *INTEGRAL* as part of the AO-1 open time program. This monitoring continued in AO-2 and AO-3. Here we present the results of the very first satellite revolution (48) of our monitoring program. The observation lasted for a continuous 100 ksec. We also had a simultaneous campaign with *RXTE* to complement our *INTEGRAL* observations. *RXTE* observed GRS 1915+105 for about one-third of the *INTEGRAL* time. (See Hannikainen et al. 2005 for details of the observations and data reduction). The JEM-X lightcurve from the whole observation is shown in Figure 5, and superposed is the duration of the *RXTE* observation.

3.2 A New Type of Variability?

Throughout most of the JEM-X lightcurve we see a novel class of variability, characterized by 5-minute pulses, not observed before (Hannikainen et al. 2003). The entire JEM-X lightcurve is dominated by these 5-min pulses, as evidenced by 3 mHz quasi-periodic oscillation which resulted from a Fourier transform of the whole JEM-X lightcurve (Hannikainen et al. 2003). Although this kind of pulsed variability resembles the ρ-heartbeat and κ oscillations (Belloni et al. 2000), the oscillations presented there are more uniform and occur on shorter timescales.

3.2.1 RXTE and "Pulses"

During some of the *RXTE* pointings, the 5-min pulses are clearly detected also by *RXTE*/PCA (Fig. 6 left). In one segment in particular, we see nine consecutive pulses, representative of the variability pattern in the majority of the JEM-X lightcurve.

The *RXTE*/PCA lightcurve was divided into three energy bands (2–5, 5–13, 13–40 keV) and smoothed with a boxcar average of 5 time bins. Fig. 6 (right) shows the mean of the nine *RXTE*/PCA pulses. The pulses consist of the main pulse (with the rising phase being shorter and harder than the declining phase) and a precursor pulse, which is shorter, softer, and of smaller amplitude then the main pulse. We can see that the rising phase of the (main) pulse is harder than the declining phase. In addition, the rise is also shorter than the decline. In each of these nine pulses there is also a precursor seen only in the softer X-ray bands.

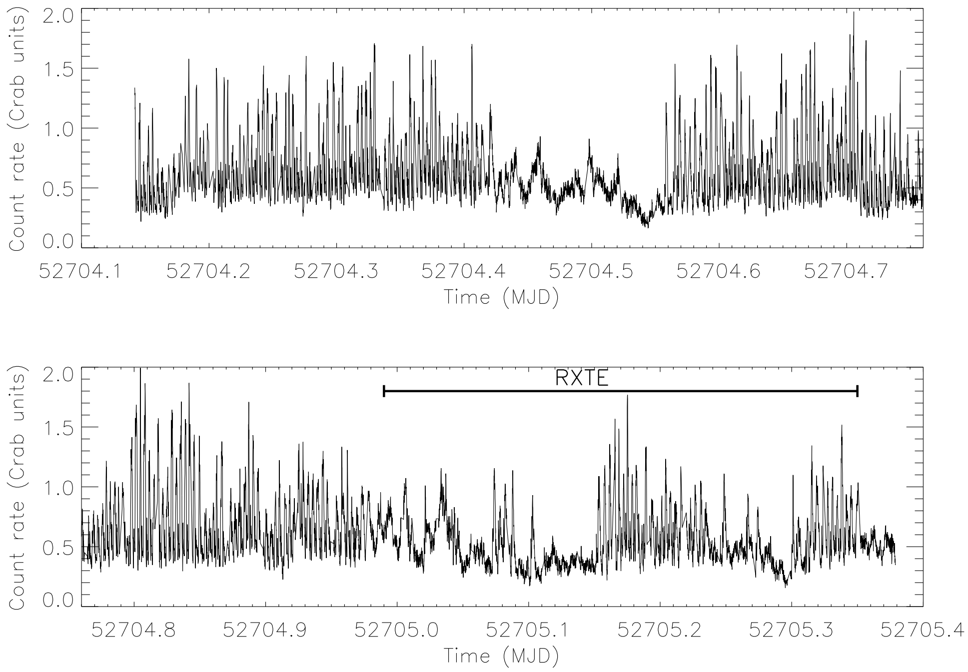

Fig. 5 The JEM-X 3–35 keV lightcurve for the whole of Rev. 48. The time bin is 8 s. As can be seen, the source varied between ~0.25–2 Crab. Shown on the plot is our simultaneous *RXTE* coverage.

The continuous 100 ksec observations, thanks to *INTEGRAL's* eccentric orbit, allowed us classify this new type of variability. In concordance with Belloni et al.'s (2000) classification system for the different forms of variability observed in the X-ray lightcurves of GRS 1915+105, we call this new type ξ. This variability, characterized by 5-minute pulses, dominated the JEM-X lightcurve, and was also observed by *RXTE*/PCA. The rising phases of the pulses are are harder and shorter than declining phases, contrary to what is seen in the ρ and κ classes of Belloni et al. (2000). Also the rise is shorter than the decline, contrary to the κ class which were interpreted as a sudden disappearance of the inner disk following a slower filling-in of the inner disk regions. The ξ-class pulses are more flare-like and may be due to strong flaring of the inner disk.

3.2.2 INTEGRAL and the Hybrid Model

In this section, we will introduce the hybrid model used to fit the *INTEGRAL* spectra. In order to conduct a detailed analysis of the spectrum, we used the co-added spectra, extracted from the high and low flux parts in the *INTEGRAL* lightcurve – data above 70 counts s^{-1} (~0.5 Crab) contributed to the "high" part, while data below 70 counts s^{-1} contributed to the "low" part. This provided us with two broadband spectra (JEM-X + ISGRI + SPI) in the energy range 3–200 keV, for the pulse maxima and minima separately. The two spectra were fitted using XSPEC V11.3 (Arnaud 1996). We interpret the spectra in terms of Comptonization of soft X-ray seed photons, assumed here to be a disk blackbody with a maximum temperature, T_{in}. We use the `eqpair` Comptonization model by Coppi (1992, 1999).

In the `eqpair` model, the electron distribution can be set to be purely thermal Maxwellian or a hybrid consisting of a Maxwellian component and a higher energy component. The introduction of the latter component is to take into account the situation where the presence of an acceleration process will give rise to a high-energy tail in addition to a normal Maxwellian distribution. The electron distribution, including the temperature (T_e) is calculated self-consistently from the assumed form of the acceleration (if present) and

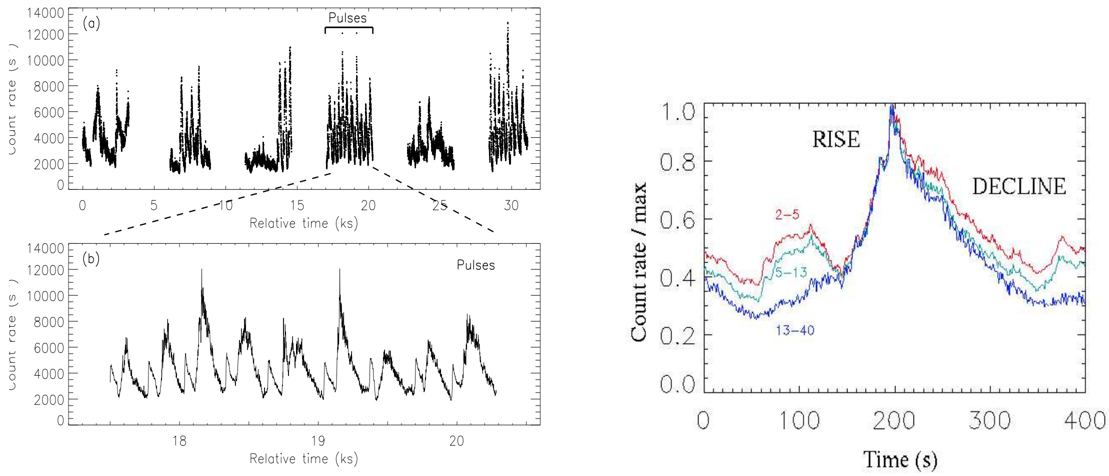

Fig. 6 *Left.* (a) The *RXTE*/PCA 2.5–15 keV lightcurve (time bin 1s). Each segment represents one *RXTE* orbit. (b) An expanded plot of the pulses. *Right.* The mean of the nine *RXTE*/PCA pulses. The lines are as follows: top (red) – 2–5 keV; middle (cyan) – 5–13 keV; bottom (blue) – 13–40 keV.

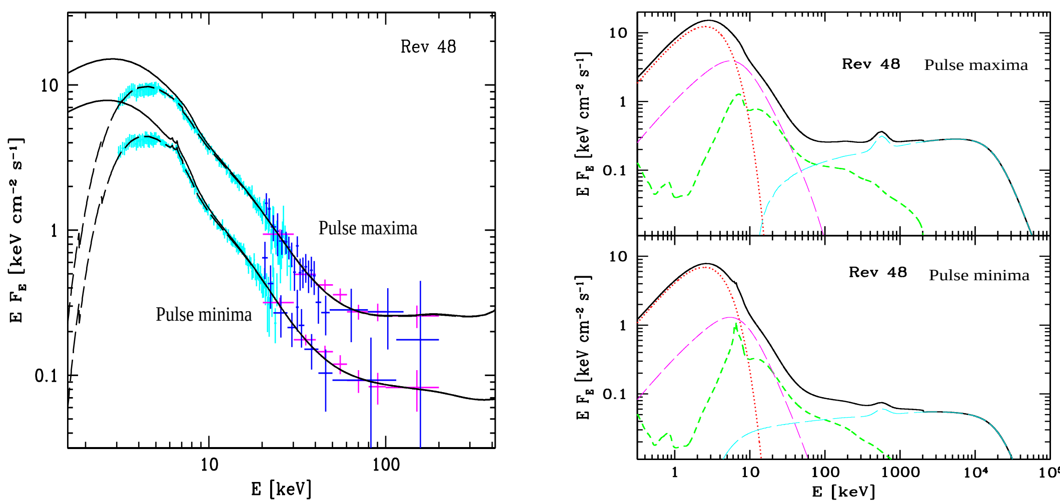

Fig. 7 *Left.* Deconvolved spectra of GRS 1915+105 during Revolution 48 from the pulse maxima (top) and pulse minima (bottom). The cyan, magenta and blue datapoints are from JEM-X, ISGRI and SPI, respectively. The dashed and solid curves represent the best-fit models to the observed and unabsorbed spectra respectively. *Right.* Spectral components of the fits to the pulse maxima (upper panel) and pulse minima (lower panel). The dotted and long-dashed curves show the unscattered blackbody, and Compton scattering from thermal (red) and non-thermal (cyan) electrons, including a component from $e^{\pm}$ pair annihilation, important around 511 keV. The short-dashed curve (green) shows the component from Compton reflection, including the Fe Kα line.

from the luminosities corresponding to the plasma heating rate, L_h, and to the seed photons irradiating the cloud, L_s. The total plasma optical depth, τ, includes contributions from electrons formed by ionization of the atoms in the plasma, τ_i (which is a free parameter) and contribution from $e^{\pm}$ pairs, $\tau - \tau_i$ (which is calculated self-consistently by the model). The importance of pairs and the relative importance of Coulomb scattering depend on the ratio of the luminosity, ℓ, to the characteristic size, r, which is usually expressed

Table 1 Model parameters[a] for the best-fit models to the broadband spectra for the co-added pulse maxima and minima

Data	$N_{\rm H}$ 10^{22} cm^{-2}	$kT_{\rm in}$ keV	ℓ_h/ℓ_s	ℓ_{nth}/ℓ_{th}	$\Gamma_{\rm inj}$	$\tau_{\rm i}$	$\tau^{\rm b}$	$kT_{\rm e}^{\rm b}$ keV	$F_{\rm bol}{}^{\rm c}$ erg cm^{-2} s^{-1}
Pulse maxima	$5.4^{+0.7}_{-0.9}$	$1.07^{+0.10}_{-0.40}$	$0.21^{+0.03}_{-0.02}$	$0.26^{+0.02}_{-0.07}$	$1.0^{+0.2}_{-0.9}$	$0^{+0.63}$	0.50	28.5	5.8×10^{-8}
Pulse minima	$6.4^{+1.4}_{-0.9}$	$1.05^{+0.08}_{-0.24}$	$0.12^{+0.03}_{-0.01}$	$0.21^{-0.11}_{+0.04}$	$1.9^{+0.6}_{-0.5}$	$0.18^{+0.20}_{-0.15}$	0.34	34.4	2.9×10^{-8}

[a] The uncertainties are for 90% confidence, i.e., $\Delta\chi^2 = 2.71$.
[b] Calculated from the energy and pair balance, i.e., not a free fit parameter.
[c] The bolometric flux of the unabsorbed model spectrum.

in dimensionless form as the compactness parameter, $\ell \equiv L\sigma_{\rm T}/(rm_{\rm e}c^3)$, where $\sigma_{\rm T}$ is the Thomson cross section and $m_{\rm e}$ is the electron mass. The compactness corresponding to the electron acceleration at a power-law rate with an index, $\Gamma_{\rm inj}$ and to a direct heating (i.e. in addition to Coulomb energy exchange with non-thermal $e^\pm$ and Compton heating) of the thermal $e^\pm$ are denoted as ℓ_{nth} and ℓ_{th} respectively, and $\ell_h = \ell_{nth} + \ell_{th}$.

Following Zdziarski et al. (2001), we assume here a constant $\ell_s = 100$, compatible with the high luminosity of GRS 1915+105. For example, for half of the Eddington luminosity, L_E, and spherical geometry, the size of the plasma corresponds to $r \sim 100GM/c^2$. We note, however, that the dependence of the fit on ℓ_s is rather weak, as this parameter is important only for $e^\pm$ pair production and Coulomb scattering, with the former not constrained by our data and latter only important at $l_s \lesssim 1$ or so.

We include Compton reflection parametrized by an effective solid angle subtended by the reflector as seen from the hot plasma, Ω, and an Fe Kα fluorescent line from an accretion disk assumed to extend down to $6GM/c^2$, the radius of the last stable orbit for particles around a Schwarzschild black hole. We assume a temperature of the reflecting medium of 10^6 K, and allow it to be ionized. We define the ionizing parameter as $\xi_{\rm ion} \equiv 4\pi F_{\rm ion}/n$, where $F_{\rm ion}$ is the ionizing flux and n is the reflector density. As the data poorly constrain $\xi_{\rm ion}$, but clearly require the reflector to be ionized, we freeze it to a value of 100 erg cm s^{-1}, in the middle of the confidence intervals for both fits. We further assume the elemental abundances of Anders & Ebihara (1982), an absorbing column of $N_{\rm H} \geq 1.8\times10^{22}$ cm^{-2}, which is an estimate of the Galactic column density in the direction of the source by Dickey & Lockman (1990), and an inclination of 66° (Fender et al. 1999). (For details of original sources and full results, see Hannikainen et al. 2005).

We will present the results only briefly here. The two spectra are shown in Fig. 7 (left) together with the best-fit model. The parameters for the best-fit model are given in Table 1. Figure 7 (right) shows the spectral components of the fits of the two spectra. Note that the small values of χ^2 – 87/191 for the pulse maxima and 93/176 for the pulse minima – are due to the systematics assumed for the *INTEGRAL* data.

Figure 7 shows that the main difference between the pulse maxima and pulse minima is in the observed flux, which is higher by a factor of $\simeq$2 during maxima. Both spectra show that GRS 1915+105 during Revolution 48 was in a soft state, with spectra similar to those of state A in Sobolewska & Życki (2003) and in between the softest spectrum of the variability class C/χ and that in the B/γ class, as observed by *RXTE* and *CGRO*. The fits imply that during pulse maxima as well as minima the spectrum $\lesssim$6 keV is dominated by unscattered disk emission, with Comptonized emission dominating only at higher energies, and including a significant contribution from non-thermal electrons. The figure shows scattering by thermal and non-thermal electrons separately. We see that there is a significant softening of the Comptonized part of the spectrum during pulse minima, which is compatible with Fig. 6 (right). This is reflected in the ratio, ℓ_h/ℓ_s, being significantly smaller. The ratio ℓ_h/ℓ_s, or, equivalently, $L_{\rm h}/L_{\rm s}$, is between the power supplied to the electrons in the Comptonizing plasma and that in soft disk blackbody photons irradiating the plasma. Our fits do not require an additional component in soft photons not irradiating the hot plasma and thus $L_{\rm s}$ corresponds to the luminosity in the entire disk blackbody emission. As implied by the value of the bolometric flux in Table 1, the value of $L_{\rm s}$ (which dominates the bolometric flux) decreases by a factor of $\simeq 2$ during minima. Given the corresponding decrease of $L_{\rm h}/L_{\rm s}$ by a factor of $\simeq 2$, we find that $L_{\rm h}$ decreased by ~ 4. Conversely, there is an increase in the relative power supplied to the electrons in the plasma during pulse maxima by a factor of $\sim$2. It should be noted that the spectrum from the pulse maxima contains both the end of the rising phase and the beginning of the declining phase of each pulse, and thus it is an average of the harder rising and the softer declining phases.

3.2.3 Summary

Broadband spectral modelling of the co-added spectra for the pulse maxima and minima respectively, using `eqpair`, showed that the spectra of the maxima and the minima both belong to spectral class A, according to the classification of Belloni et al. (2000), and were essentially similar, except for a significant softening of the Comptonized part of the spectrum during the minima. The fact that the spectra do not change between pulse maxima and pulse minima (except for the flux level) and that the pulses are described by a fast rise and a slow decline indicates that the variability is not representative of oscillations between spectral states (as e.g. class ρ in Belloni et al. 2000). The variability could result from flares in the accretion disk arising from instabilities in the accretion rate.

4 CONCLUSIONS

We have shown here how we can derive important information on microquasars from two very different wavelength extremes. The radio shows us how GRO J1655$-$40 really behaves like a *micro*-quasar, while the X-ray/gamma-ray allows us to probe deep into the innards of these objects.

Acknowledgements DCH and LH acknowledge support from the Academy of Finland. This work was supported in part by the NORDITA Nordic Project on High Energy Astrophysics and by the HESA/Antares program of the Academy of Finland and TEKES, the Finnish Technology Agency. Based on observations with *INTEGRAL*.

References

Arnaud, K., 1996, ASP COnf. Ser. 101, 17
Belloni, T., et al., 2000, A&A, 355, 271
Blandford, R.D., & Königl, A., 1979, ApJ, 232, 34
Castro-Tirado, A.J, Brandt, S., & Lund, N., 1992, IAUC, 5590
Coppi, P.S., 1992, MNRAS, 258, 657
Coppi, P.S., 1998, ASP Conf. Ser., 161,375
Dickey, J.M., & Lockman, F.J., 1990, ARA&A, 28, 215
Fender, R.P., et al., 1999, MNRAS, 304, 865
Gallo, E., Fender, R.P., & Pooley, G.G., 2003, MNRAS, 344, 60
Gear, W.K., et al., 1994, MNRAS, 267, 167
Giacconi, R., Gursky, H., Paolini, F., & Bruno Rossi, 1962, Physical Review Letters, 9, 439
Greiner, J., et al., 2001, A&A, 373, L37
Hannikainen, D.C., Hunstead, R.W., Campbell-Wilson, D., & Sood, R.K., 1998, A&A, 337, 460
Hannikainen, D.C. et al., 2000, ApJ, 540, 521
Hannikainen, D.C., et al., 2005, A&A, 435, 995
Harlaftis, E., & Greiner, J., 2004, A&A, 414, L13
Hjellming, R.M., & Johnston, K.J., 1988, ApJ, 328, 600
Hjellming, R.M., & Rupen, M.P., 1995, Nature, 375, 464
Macquart, J.-P., Wu, K., Sault, R.J., & Hannikainen, D.C., 2002, A&A, 396, 615
Marscher, A.P., & Gear, W.K., 1985, ApJ, 298, 114
Mirabel, I.F., & Rodríguez, L.F., 1998, Nature, 392, 673
Orosz, J.A., & Bailyn, C.D., 1997, ApJ, 477, 876
Rodríguez, L.F., & Mirabel, I.F., 1999, ApJ, 511, 398
Sobolewska, M.A., & Życki, P.T., 2003, A&A, 400, 553
Soria, R., Wickramasinghe, D.T., Hunstead, R.W., & Wu, K., 1998, ApJ, 495, L95
Stevens, J.A., Hannikainen, D.C., Wu, K., Hunstead, R.W. & McKay, D.J., 2003, MNRAS, 342, 623
Valtaoja, E.,et al., 1992, A&A, 254, 71
van der Laan, H., 1966, Nature, 211, 1131
Winkler, C., et al., 2003, A&A, 411, L1
Zdziarski, A.A., Grove, J.E., Poutanen, J., Rao, A.R., & Vadawale, S.V., 2001, ApJ, 554, L45